On the ferromagnetic structure of the intermetallic borocarbide $TbCo_2B_2C$

2009 J. Phys.: Condens. Matter 21 216006

(http://iopscience.iop.org/0953-8984/21/21/216006)

J. Phys.: Condens. Matter **21** (2009) 216006 (9pp) doi:10.1088/0953-8984/21/21/216006

On the ferromagnetic structure of the intermetallic borocarbide $TbCo_2B_2C$

M ElMassalami[1], R Moreno[1], R M Saeed[1], F A B Chaves[1], C M Chaves[1], R E Rapp[1], H Takeya[2], B Ouladdiaf[3] and M Amara[4]

[1] Instituto de Fisica, Universidade Federal do Rio de Janeiro, Caixa Postal 68528, 21945-970 Rio de Janeiro, Brazil
[2] National Institute for Materials Science, 1-2-1 Sengen, Tsukuba, Ibaraki 305-0047, Japan
[3] Institut Laue-Langevin, BP 156, F-38042 Grenoble Cedex 9, France
[4] Institut Néel—CNRS, Bâtiment D, BP 166, F-38042 Grenoble Cedex 9, France

Received 17 December 2008, in final form 24 March 2009
Published 30 April 2009
Online at stacks.iop.org/JPhysCM/21/216006

Abstract

Based on magnetization, specific heat, magnetostriction and neutron-diffraction studies on single-crystal $TbCo_2B_2C$, it is found out that the paramagnetic properties, down to liquid nitrogen temperatures, are well described by a Curie–Weiss behavior of the Tb^{3+} moments. Furthermore, below $T_c = 6.3$ K, the Tb sublattice undergoes a ferromagnetic (FM) phase transition with the easy axis being along the (100) direction and, concomitantly, the unit cell undergoes a tetragonal-to-orthorhombic distortion. The manifestation of an FM state in $TbCo_2B_2C$ is unique among all other isomorphous borocarbides, in particular $TbNi_2B_2C$ ($T_N = 15$ K, incommensurate modulated magnetic state) even though the Tb ions in both isomorphs have almost the same crystalline electric field properties. The difference among the magnetic modes of these Tb-based isomorphs is attributed to a difference in their exchange couplings which are in turn caused by a variation in their lattice parameters and in the position of their Fermi levels.

(Some figures in this article are in colour only in the electronic version)

1. Introduction

Whenever a family of compounds, containing 3d transition metal (M) and magnetic rare-earth (R) atoms, manifests similar band structures, the trend in their magnetic properties can be rationalized in terms of the position of the Fermi level E_F within the density of states $N(E)$ curve. The RM_2 family of compounds provides the best illustration [1–4]. Here, it is commonly considered that the R moments are localized while the M moments, if they exist, are itinerant. Assuming further that the mutual interactions among the magnetic ions can be described within the molecular field theory and, in addition, using Landau phase-transition arguments together with Stoner and Wohlfarth–Rhodes criteria, then the magnetic properties of the whole RM_2 family can be classified according to the first few energy derivatives of $N(E)$ evaluated at E_F [1–4]. This model is successful in explaining the type of magnetic phase transition, the relative magnitude of the critical temperature and, moreover, the magnetic character of the 3d subsystem. The above-mentioned discussion is applicable also to the family of ternary compounds RM_2X_2 (X = Si, Ge, B) [5] and is expected to hold also for the quaternary borocarbides RM_2B_2C family (see, e.g., [6] and references therein). Although the application of such a discussion is of interest for the understanding of the magnetism (and superconductivity) of the latter family, there are only a very few studies bearing on this subject and these are mostly limited to the RNi_2B_2C series [6].

Extensive studies have also been carried out on intermetallic families with nonmagnetic R subsystem such as RT_2 [1] and RT_2X_2 [5] (R = Lu or Y, T = Ni or Co, X = Si, Ge or B). $LuCo_2$ and YCo_2, as particularly relevant examples, were shown to be exchange-enhanced paramagnets at low temperatures but manifest Curie–Weiss behavior at higher temperatures: features that are in accord with the description of the spin fluctuation model. Similarly, YCo_2B_2C was reported to show exchange-enhanced paramagnetism [7] though the isomorphous YNi_2B_2C is magnetically inactive [6]. In accord with the above-mentioned model, electronic structure calculations [8–11] on RNi_2B_2C (R = Lu, Y) showed that E_F is situated at the top of a pronounced and narrow $N(E)$ peak and this peak lies on the top edge of nearly filled Ni(3d)

bands. On the other hand, the band structure calculations [8] on $LuCo_2B_2C$ showed that, for such isomorphous RT_2B_2C, the rigid band model yields a reasonable description of the band filling. Furthermore, for $LuCo_2B_2C$, E_F is situated at the decreasing but right-hand side of one of the peaks that receives a considerable contribution from the Co 3d band, and that $N(E_F)$ is of the same magnitude as that of $LuNi_2B_2C$: the latter finding is consistent with the observation that the Sommerfeld linear specific heat coefficients of YCo_2B_2C and YNi_2B_2C are equal [12]. Moreover, as the first derivatives of $N(E)$ are nonnegligible, then we expect the Co sublattice, similar to RCo_2, to develop a spin fluctuation character at lower temperature (or even to be polarized, if the internal field at the Co site $H_{\rm eff}^{\rm Co}$ is stronger than the critical field $H_{\rm cr}^{\rm Co}$): the spin fluctuation character was indeed reported for YCo_2B_2C [7, 13].

As is evident from the above, the difference in the position of E_F within each of RNi_2B_2C and RCo_2B_2C is reflected as a difference in, for example, their magnetic properties [7, 12] such as the magnetic structure. As the magnetic properties of RNi_2B_2C are well documented [6], it is then of interest to investigate the magnetic structures of the RCo_2B_2C series and, moreover, to elucidate the interplay between the magnetism of their R and M subsystems. Along these objectives, this paper reports on the extensive magnetic characterization of $TbCo_2B_2C$. The successful synthesis of a single crystal of $TbCo_2B_2C$ made it possible to identify unambiguously the paramagnetic as well as the ordered-state properties of the Tb sublattice: the former is dominated by a Curie–Weiss behavior while the latter is characterized by a ferromagnetic structure with the easy axis lying along the a direction. This work also addressed the question of whether the surge of this FM state (with an expected strong $H_{\rm eff}^{\rm Co}$) is able to polarize the Co 3d subsystem. Our results suggest that, in spite of the intermediate character of the Co 3d subsystem, there is no unambiguous evidence that supports a surge of spontaneous polarization.

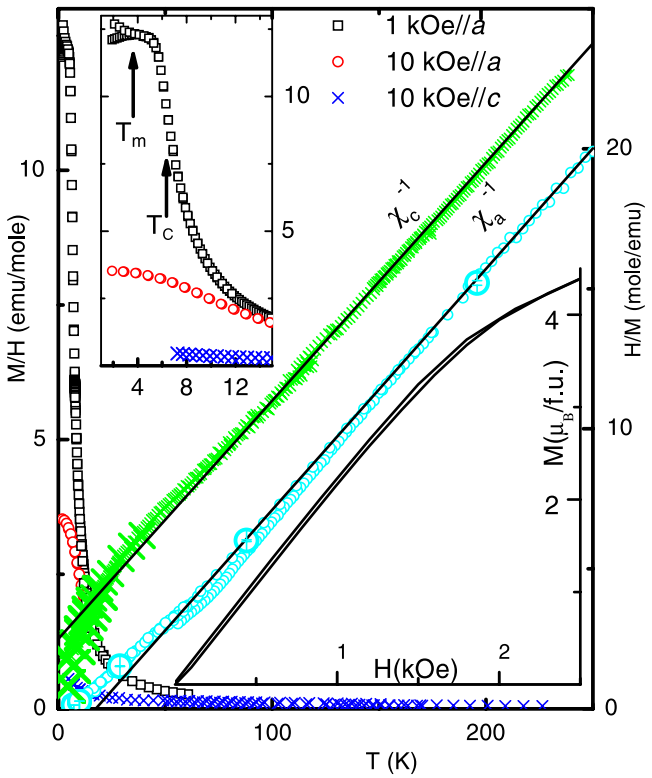

Figure 1. T-dependent $\chi_{\rm dc}$ (left-hand ordinate) and $\chi_{\rm dc}^{-1}$ (right-hand ordinate) curves of $TbCo_2B_2C$ measured along the a and c axes. The solid lines represent $\chi = C/(T-\theta)$; C and θ are the Curie–Weiss constants. The large symbols on the $\chi_{\rm dc}^{-1}(T)$ curves represent the $H/M(T, H \to 0)$ as obtained from the Arrot plot. The upper-left inset shows, on expanded scales, the low-temperature $\chi_{\rm dc}(T, H \parallel a)$ for $H = 1$, 10 kOe and $\chi_{\rm dc}(T, H \parallel c)$ for $H = 10$ kOe. The lower-right inset shows part of the magnetization isotherms at $T = 1.9$ K (see figure 2) which demonstrates that, for $H \geqslant 2$ kOe, there is no hysteresis effect (see the text).

2. Experiment

99.5% ^{11}B-enriched polycrystals of $TbCo_2B_2C$ were prepared by the conventional arc-melt method. These polycrystals were used as feeding rods during a floating-zone synthesis, a process that we used for single-crystal growth [14].

Characterization were carried out using magnetization ($M(T, H)$, extraction method, 1.9 K $\leqslant T \leqslant$ 300 K, $H \leqslant$ 90 kOe) and zero-field specific heat ($C(T)$, semi-adiabatic method, 0.5 K $\leqslant T \leqslant$ 15 K, accuracy better than 4%). A high accuracy capacitance dilatometer [15] was used for measuring the thermal expansion or forced magnetostriction with a resolution better than 1 Å. The relative change in length, measured along the cosine directions ($\beta_1\beta_2\beta_3$) when a field is applied along the cosine direction (xyz), is denoted as ${}^{\beta_1\beta_2\beta_3}\lambda_{xyz}(T) = [l(T, H) - l_0(T_0, H_0)]/l_0(T_0, H_0)$.

Neutron-diffraction measurements were carried out at the Institut Laue-Langevin in Grenoble, France on a powdered as-prepared arc-melt polycrystalline sample (since a large quantity is desirable, see section 3.4 below) as well as on a single-crystal sample. The powder diffraction patterns were collected within a temperature range 2–40 K using the D1B diffractometer with a selected incident wavelength of 2.42 Å; Rietveld refinements of both crystallographic and magnetic structures were carried out using the FULLPROF package of Rodriguez-Carvajal (www.ill.fr/dif/Soft/fp). Single-crystal diffraction studies were performed on the D10 four-circle diffractometer with $\lambda = 2.3606$ Å over a wide range of q space and within the temperature range 1.7 K $< T <$ 8 K.

3. Results

3.1. Magnetization

Figure 1 shows the T-dependent $\chi_{\rm dc}$ and $\chi_{\rm dc}^{-1}$ curves that were measured at different fields and along the two principal tetragonal axes. The large symbols on the $\chi_{\rm dc}^{-1}(T)$ curve represent the $H/M(T, H \to 0)$ obtained from the Arrot plot: the excellent agreement emphasizes that, within this temperature range, the contribution of magnetic impurities is negligible. A Curie–Weiss fit down to liquid nitrogen temperatures of $\chi_{\rm dc}(T, H \parallel c)$ gives $\mu_{\rm eff} = 9.7(1)\ \mu_B$ and $\theta_c = -29.4(1)$ K while that of $\chi_{\rm dc}(T, H \parallel a)$ gives $\mu_{\rm eff} = 9.6(1)\ \mu_B$ and $\theta_a = 14.4(1)$ K. Evidently, there are anisotropic forces but the effective moments are in excellent agreement

with the value expected for a free Tb^{3+} ion. Based on these anisotropic θ values, the first Stevens coefficient in the crystal field description of a tetragonal symmetry is estimated to be $B_2^0 = 0.88(2)$ K; this compares well in sign and magnitude with that of $TbNi_2B_2C$ ($B_2^0 = 1.2(1)$ K) [15]. This similarity suggests that the crystalline electric fields, CEF, at the Tb^{3+} site of both isomorphs are similar: indeed, both sites have the same D_{4h} symmetry and almost the same charge distribution. On lowering the temperatures toward the liquid helium region, $\chi_{dc}(T, H \parallel a)$ increases relatively fast and afterward tends toward saturation. Considering the characteristic magnetic features manifested in the magnetization, specific heat and neutron diffraction (see below), this rapid increase (which is followed by saturation) is due to the approach and eventual onset of an FM order wherein the moments point along the a axis: $T_c = 6.3(2)$ K is the point of maximum inclination.

The upper-left inset of figure 1 shows, on an expanded scale, a magnetic hysteresis occurring at $T \leqslant T_m = 3.7(2)$ K and $H = 1$ kOe. The $M(H \parallel a, 1.9\ \text{K})$ curve, shown in the lower-right inset of figure 1, reveals that this hysteresis effect disappears for $H \geqslant 2$ kOe. Since this T_m feature is sample-dependent (see below), it is attributed to a contaminating magnetic phase, the magnetization of which saturates completely to 0.05 μ_B/f.u. for $H \geqslant 2$ kOe. Based on the weight ratios of the magnetic moments, the fraction of the Tb ions in this spurious phase relative to the major $TbCo_2B_2C$ phase is estimated to be 0.7%.

Figure 2 confirms the above-mentioned magnetic anisotropy, due to which the $a(c)$ is the easy (hard) axis. Within the studied ranges of H and T, the magnetization isotherms do not show any field-induced transition; rather, only a monotonic and steady increase (tending towards saturation) which is characteristic of a forced domain alignment: this supports the earlier inference of an FM order. Furthermore, the magnetization above 60 kOe increases as $M(60 \leqslant H \parallel a \leqslant 90\ \text{kOe}, 2\ \text{K}) = \mu_{sp} + \chi_{hf}H$ ($\mu_{sp} = 7.6(3)\mu_B$, $\chi_{hf} = 6.8(4) \times 10^{-6}$ μ_B Oe^{-1} corresponding to $38(2) \times 10^{-3}$ emu mol^{-1}) attaining $\mu(90\ \text{kOe}, 2\ \text{K}) = 8.2$ μ_B. μ_{sp} is only 3% lower than the moment reported for $TbNi_2B_2C$ ($\mu_{Tb} = 7.78$ μ_B [16, 17]), but 16% lower than the one expected for a free Tb^{3+} ion: such a lowering confirms the above-mentioned influence of the CEF effects and that these effects are similar to the ones observed in the Ni-based isomorph. Alternatively, let us assume that the difference between μ_{sp} of $TbCo_2B_2C$ and the reported moment of $TbNi_2B_2C$ is due exclusively to the spontaneous polarization of the Co 3d orbitals which are coupled ferrimagnetically to the FM ordered Tb sublattice. Then, based on the relation $\mu_{sp}(TbCo_2B_2C) = \mu_{sp}(TbNi_2B_2C) - 2\mu_{Co}$, the maximum possible Co moment would be $\mu_{Co} = 0.25$ μ_B amounting to only 0.25 hole/Co atom in the 3d band; such a value is almost one-fourth of the Co moment encountered in the heavy members of the RCo_2 series [18]. It is more likely that there is no spontaneous or field-induced Co polarization since, if there is any, then the induced moment would be much higher than 0.25 μ_B. In addition, as the CW law describes very well the paramagnetic susceptibility of $TbCo_2B_2C$ up to 300 K, then within this range the exchange-enhancement factor for the Co subsystem susceptibility must be relatively small. Evidently high-temperature magnetization is needed to address the question of the spin fluctuation character of Co in $TbCo_2B_2C$.

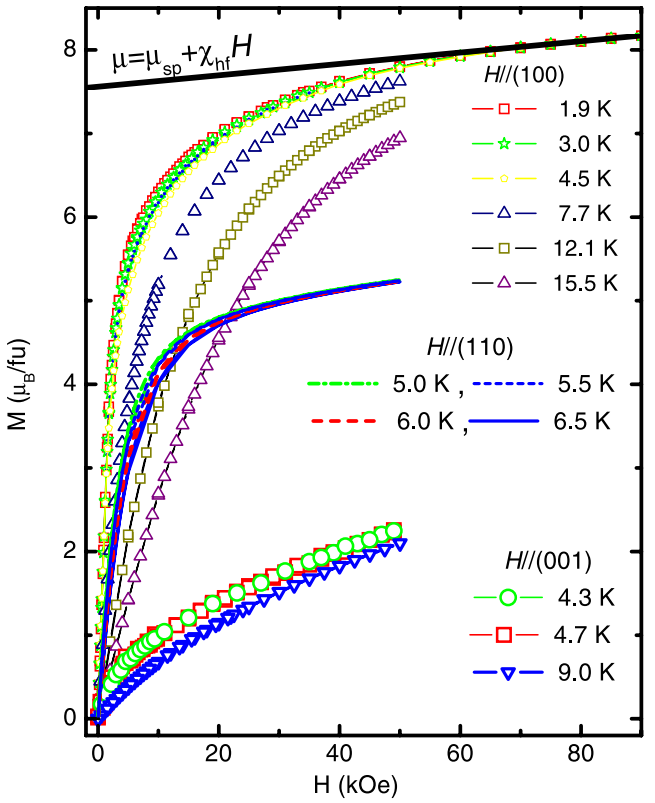

Figure 2. Magnetization isotherms of $TbCo_2B_2C$ at different temperatures and for different field orientations. Two different set-ups were employed, one with a field up to 90 kOe and another up to 50 kOe. The high-field magnetization ($H > 60$ kOe) evolves as $M(H \parallel a, 2\ \text{K}) = \mu_{sp} + \chi_{hf}H$ and is represented by the solid line (see the text).

3.2. Specific heat

Figure 3 shows the zero-field magnetic specific heat and entropy of single-crystal $TbCo_2B_2C$ obtained after subtracting the nuclear, electronic and lattice contributions (the latter two were obtained from YCo_2B_2C) [7, 12]. The nuclear contribution is of dominant importance only at very low temperatures and was evaluated from the diagonalization of the hyperfine Hamiltonian [19]. It is worth mentioning that, at very low temperatures, the nuclear contribution is much stronger than the magnetic one: as such, the propagation of errors due to successive subtractions of non-magnon contributions would eventually influence the absolute value of $C_M(T)$; this may undermine the quality of the comparison, at lower temperatures, between the theoretical and experimental magnon contributions (see figure 3).

Both $C_{mag}(T)$ and $S_{mag}(T)$ curves do confirm the onset of the magnetic order at T_c: the former curve rises very sharply at T_c while the latter manifests a pronounced change of slope. Considering a Tb sublattice FM order (see below), we fit the experimental $C_{mag}(T)$ to the theoretical magnon expression of equation (A.5) (see the appendix): as can be

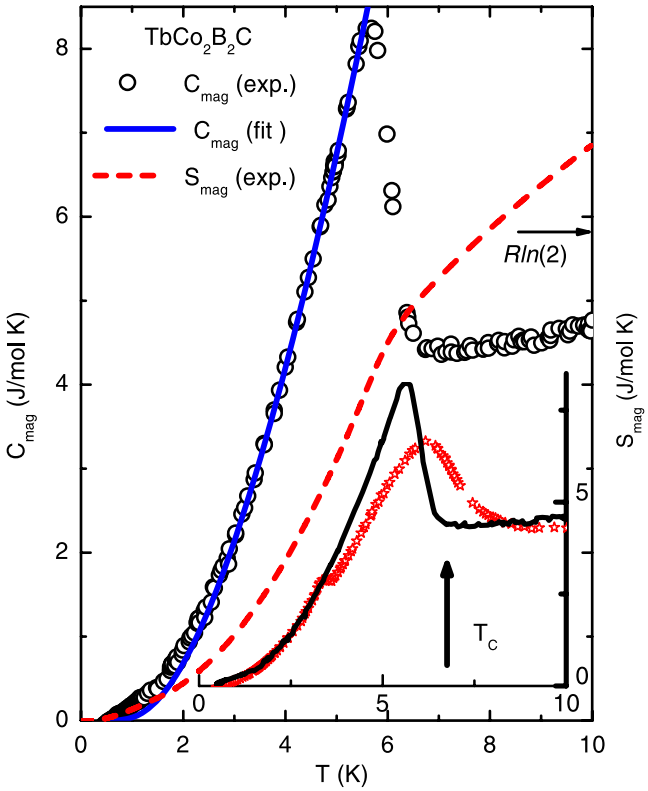

Figure 3. Zero-field magnetic specific heat (symbol) and calculated magnetic entropy (dashed line) of single-crystal $TbCo_2B_2C$. The nuclear, electronic and lattice contributions were already subtracted (the latter two were obtained from YCo_2B_2C) [7, 12]. The solid line represents a fit to the expression of the magnon contribution (equation (A.5)) assuming an FM order of the Tb sublattice. The inset compares the single-crystal magnetic specific heat (solid line) with that of a polycrystalline sample (symbol); the observed difference reflects a strong sample dependence. However, their magnetic entropies approach each other for $T > T_c$ confirming, as it should, the conservation of the total entropy (see the text).

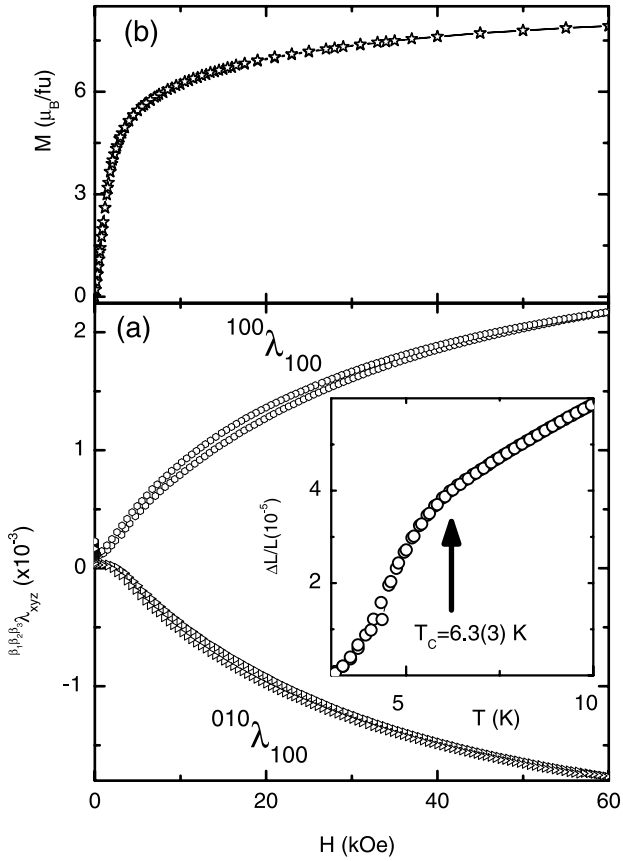

Figure 4. (a) Representative forced magnetostrictions ${}^{100}\lambda_{100}(H, 3\ \mathrm{K})$ and ${}^{010}\lambda_{100}(H, 3\ \mathrm{K})$ curves of $TbCo_2B_2C$ are compared to (b) the isothermal magnetization at 3 K. The magnetostriction curves are given relative to their zero-field values. The inset shows the thermal evolution of the zero-field $\Delta L/L$ measured along the a axis. The arrow marks the T_c value which was determined from the specific heat measurement of figure 3.

seen in figure 3, the excellent fit to equation (A.5) gives the spin-wave stiffness coefficient $D = 26.3(5)$ K and the gap parameter $\Delta = 8.4(2)$ K. The high value of D is indicative of stronger effective exchange couplings. On the other hand, the value of Δ (which from equation (A.3) is a measure of the anisotropic field) is consistent with the strong anisotropic features observed in the magnetization measurements.

The inset of figure 3 compares the measured $C_{\mathrm{mag}}(T)$ of a single-crystal sample with that of a polycrystalline one. Evidently the T_m transition is sample-dependent: while $C_{\mathrm{mag}}(T)$ of the polycrystalline sample manifests a pronounced event at $T_m = 3.6(2)$ K, that of the single crystal hardly shows any anomaly. As mentioned above, the single-crystal sample contains only a 0.7% spurious phase and this concentration limit is lower than the resolution of the specific heat set-up.

3.3. Magnetostriction

Figure 4 shows the forced magnetostriction isotherms measured along the a and b axes with $H \parallel a$. Once more (apart from the low-field, domain-wall sweeping-out region and the saturated regime) there is no (metamagnetic) transition in these isotherms. The inset of figure 4 indicates clearly that, below T_c, $TbCo_2B_2C$ undergoes a spontaneous distortion which—based on figure 4(a), see also section 3.4—is attributed to an orthorhombic distortion of the tetragonal unit cell. A similar distortion was reported for $TbNi_2B_2C$ [15, 20–23]. Then the behavior of the forced magnetostriction of figure 4 can be understood as follows: at zero field, there is an equal distribution of domains along each of the a and b axes; an applied field along, say, the a axis would involve a rearrangement of the orthorhombically distorted domains and as such induces an increase in $M(H \parallel a)$ (figure 4(b)), an increase in ${}^{100}\lambda_{100}(H)$ and a decrease in ${}^{010}\lambda_{100}(H)$ (figure 4(a)).

3.4. Neutron diffraction

The thermal evolution of the powder diffractograms is shown in figures 5 and 6. For $T > T_c$, the patterns are due to the crystal structure of $TbCo_2B_2C$ and of a small impurity phase. On the other hand, for $T_m < T < T_c$, it is evident that the magnetic reflections are piled up on the top of the nuclear Bragg peaks: a $q_0 = (000)$ mode.

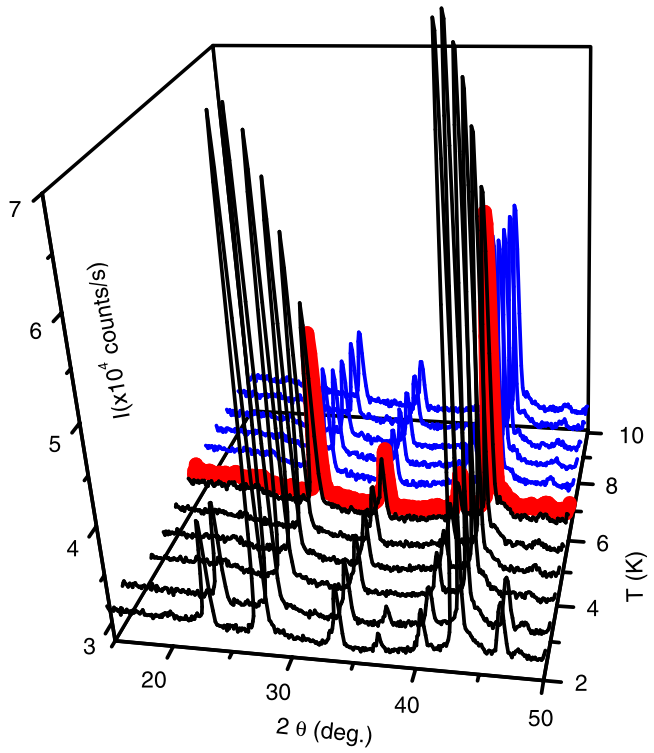

Figure 5. Representative neutron powder diffractograms of as-prepared polycrystalline $TbCo_2B_2C$. To aid in visualizing the magnetic modes, this plot is limited to temperatures below 10 K and to scattering angles lower than 50°. The diffractogram at 6.4 K (denoted by thick solid line) can be taken as a demarcation between the paramagnetic and FM phases.

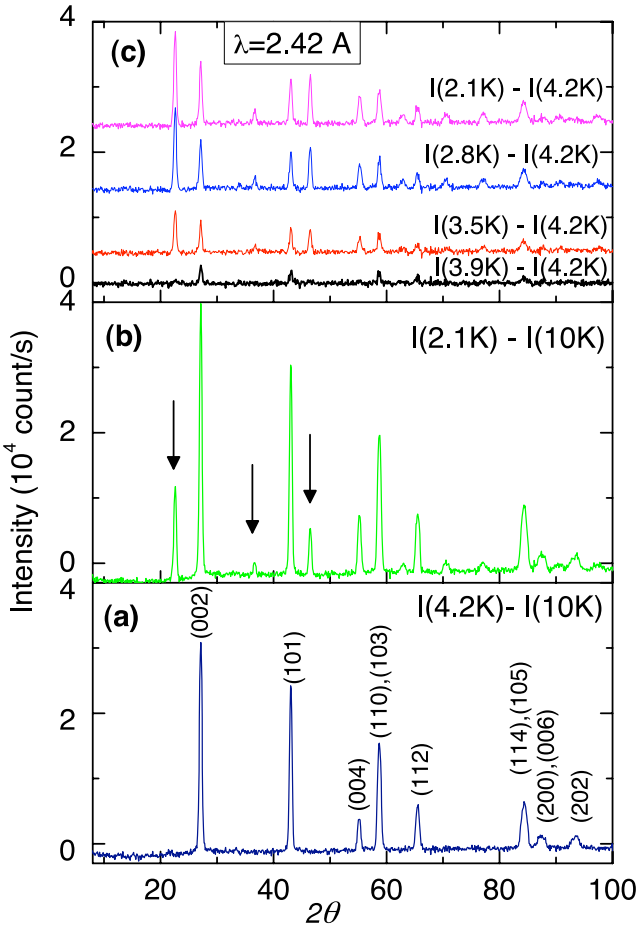

Figure 6. The magnetic diffractograms of as-prepared polycrystalline $TbCo_2B_2C$ sample. (a) The FM mode obtained after subtracting the pattern at 10 K; (b) the superposition of the FM and the magnetic contamination contributions at $T = 2.0$ K—after subtracting the pattern at 10 K—(the strongest peaks of the contamination are denoted by vertical arrows); (c) the thermal evolution ($T < T_m$) of the magnetic patterns relative to the one at 4.2 K.

Considering that the paramagnetic state is dominated by the Tb moment, that the evolution of the isothermal magnetization and magnetostriction indicates no magnetic transition which can be related to the onset of Co moment, then this q_0 mode must be related to the Tb sublattice. Furthermore, since the Tb ion occupies the special 2a site in the unit cell, then this mode must be FM, confirming the conclusions drawn from the magnetization, magnetostriction and specific heat studies. Indeed, figure 6(a) confirms that this pattern is an FM mode. Alternatively, if this mode is related to the Co sublattice then, due to the multiplicity of the 4d site occupied by the Co atoms, the magnetic order should be either AFM (if only due to Co subsystem) or ferrimagnetic (if both subsystems are ordered): in the light of all the above-mentioned results, both possibilities must be ruled out.

Below $T_m \approx 3.7$ K, the thermal evolution of the diffractograms reveals two features (figures 6(b) and (c)): first, the intensity of the FM mode evolves smoothly and independently. Second, there is a surge of additional magnetic peaks (marked by the vertical arrows in the difference plots of figures 6(b) and (c)). Since figures 1–4 do not indicate any event that can be related to an order-to-order transition of Tb magnetic structure, then these additional peaks cannot be associated with the magnetic pattern of the Tb sublattice. As these diffractograms were collected on as-prepared, arc-melt polycrystalline samples—which as mentioned above contain magnetic contamination—then these additional peaks are taken to be due to the same magnetic contamination, which is responsible for the hysteresis event in figure 1 and the weak specific heat anomaly in the inset of figure 3.

A wide range of q space within the range 1.7 K $< T <$ 8 K were scanned on a single crystal of $TbCo_2B_2C$. Indeed, most of the nuclear (and ferromagnetic) peaks that satisfy the relation $h + k + l = 2n$ were observed. In addition, we also looked, at 1.7 K, for any modulated mode within a wide q range covering $-0.4 < h < 0.6$, $-0.4 < k < 0.4$ and $-0.3 < l < 0.3$. Some weak reflections were observed. Figure 9 shows the thermal evolution of one of these peaks and, for comparison, also that of the (0, 0, 4) peak. As is evident, the intensity of the (0, 0, 4) peak, being due to magnetic and nuclear contributions, decrease smoothly and goes to the value of the nuclear intensity as the temperature reaches T_c. In particular there is no visible variation in the (0, 0, 4) intensity when T is varied across T_m, indicating that the event at this temperature does not belong to the main phase. On the other hand, the intensity of the other peak decays very fast as the temperature increases and is almost within the experimental

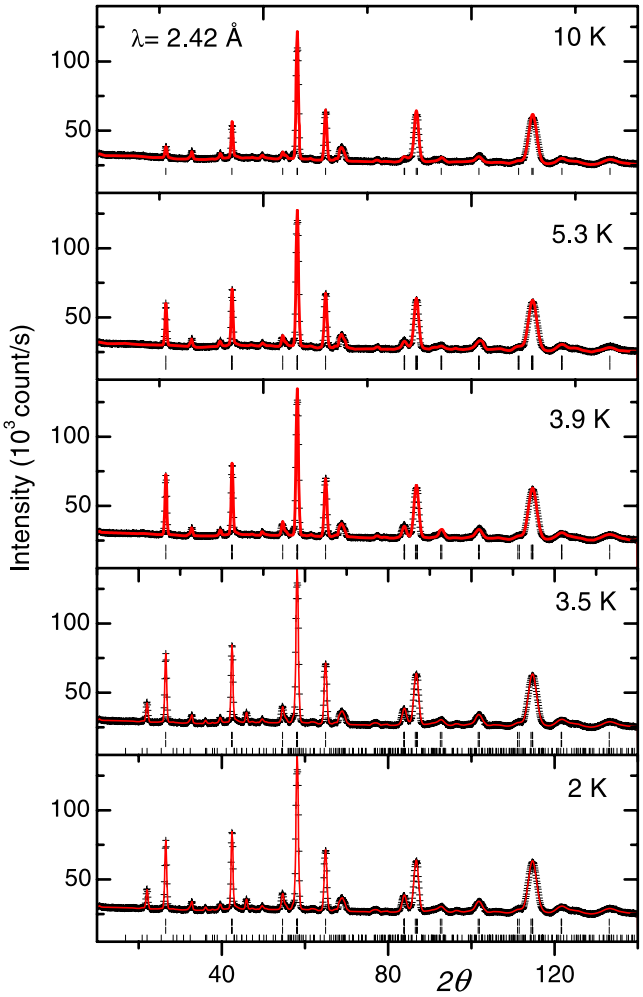

Figure 7. Rietveld analysis on representative powder diffractograms. Within the range $T_m < T < T_c$, the total contribution is composed of a nuclear and an FM component while for $T < T_m$ it is a sum of three phases: a nuclear, an FM and an impurity phase (see the text). The thermal evolution of the lattice parameters and magnetic moment are given in figure 8. The Bragg R factor for the structural phase clusters around 2 while for the magnetic phase it is around 2.1. The intensity contribution of the unidentified phase was calculated using the so-called profile matching [24]: it is emphasized that the presence of this impurity phase does not modify our conclusions regarding the magnetic properties of the $TbCo_2B_2C$ phase.

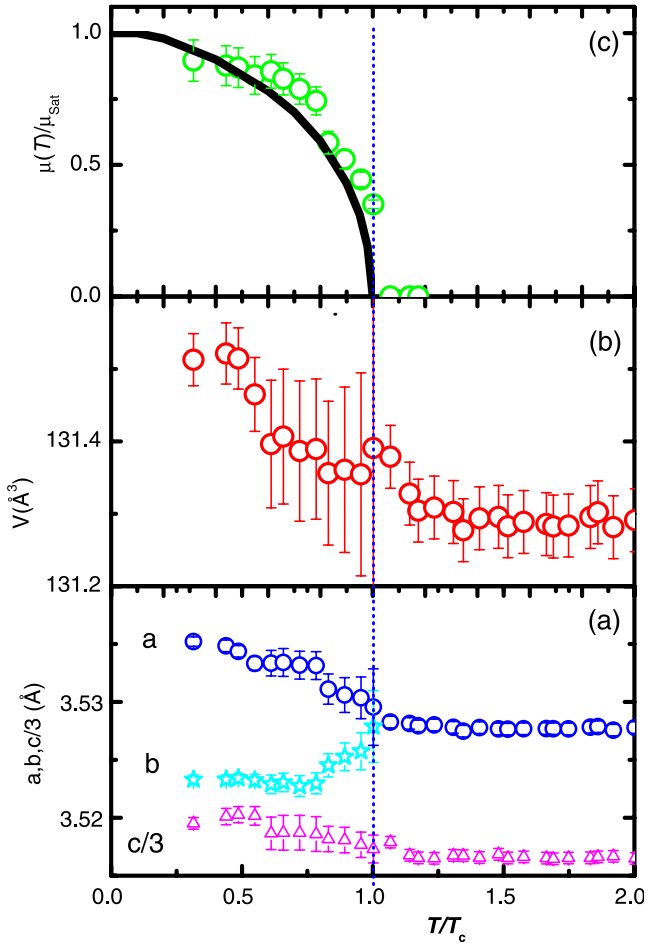

Figure 8. (a) The lattice parameters (a, b, $c/3$), (b) the unit cell volume and (c) the reduced magnetic moment $\mu(T)/\mu(2\,\mathrm{K})$ versus the reduced temperature T/T_c. These parameters were obtained from the Rietveld analysis (see figure 7). The solid line in the upper panel represents the Brillouin function with $J = 6$.

Table 1. Comparison of the space groups, atomic positions and isotropic thermal parameters of $TbCo_2B_2C$ and $TbNi_2B_2C$. The data on $TbNi_2B_2C$ are taken from Lynn *et al* [16]. The same thermal parameters reported for $TbNi_2B_2C$ are also used for the analysis of $TbCo_2B_2C$.

			Tb	Co	B	C
$TbNi_2B_2C$	$P4/mmm$	Position	(000)	$(\frac{1}{2}0\frac{1}{4})$	(0, 0, 0.357)	$(\frac{1}{2}\frac{1}{2}0)$
		Thermal factor	0.47	0.57	0.77	0.85
$TbCo_2B_2C$	$Immm$	Position	(000)	$(\frac{1}{2}0\frac{1}{4})$	(0, 0, 0.354)	$(\frac{1}{2}\frac{1}{2}0)$
		Thermal factor	0.47	0.57	0.77	0.85

uncertainty when $T > 2$ K. Such a thermal evolution is similar to the features observed in the magnetization hysteresis (figure 1), in the specific heat anomaly (inset of figure 3) and in the powder neutron diffractograms (figures 5–7). This suggests that this, as well as the other weak peaks, are related to the same impurity phase as discussed above. Evidently, the ratio of the intensity of this contaminating peak to that of the (0, 0, 4) peak is extremely small in the single-crystal sample; in terms of the above-mentioned impurity scenario, this means that the impurity concentration in the single-crystal sample is much smaller than the one in the polycrystalline case.

To extract more information, Rietveld analysis was carried out on the nuclear and magnetic patterns of the main phase. Because of the structural distortion, we used the $Immm$ space group together with the parameters given in table 1. The straightforward analysis gave a satisfactorily fit. Representative analyzed diffractograms are shown in figure 7 while the obtained cell parameters and magnetic moment are given in figure 8. The analysis indicates that the lattice parameters (figures 8(a) and (b)) undergo a noticeable orthorhombic distortion below T_c which is consistent with the magnetoelastic effects observed in figure 4. Furthermore, the lattice parameters evolve smoothly across T_m and that the mismatch parameter $(a - b)/a$ is the same as the one

Table 2. A comparison of the lattice and magnetic parameters of the isomorphous $TbCo_2B_2C$ and $TbNi_2B_2C$. The lattice parameters are reported for samples at LHe temperatures except the c parameter of $TbNi_2B_2C$; the latter was estimated by normalizing its room temperature value using the values of $HoNi_2B_2C$ [16].

	a (Å)	b (Å)	c (Å)	$\mu_{\rm eff}$ ($\mu_{\rm B}$)	$T_{\rm C,N}$ (K)	Magnetic mode	$\mu_{\rm sp}$ ($\mu_{\rm B}$)
$TbCo_2B_2C$	3.535	3.523	10.560	9.7	6.3	FM $q = (000)$	7.6
$TbNi_2B_2C$	3.554[a]	3.534[a]	10.44[b]	9.8[c]	15[c]	LSW, $q = (0.45, 0, 0)$[b]	7.78[b,c]

[a] Reference [20]; [b] Reference [16]; [c] Reference [17].

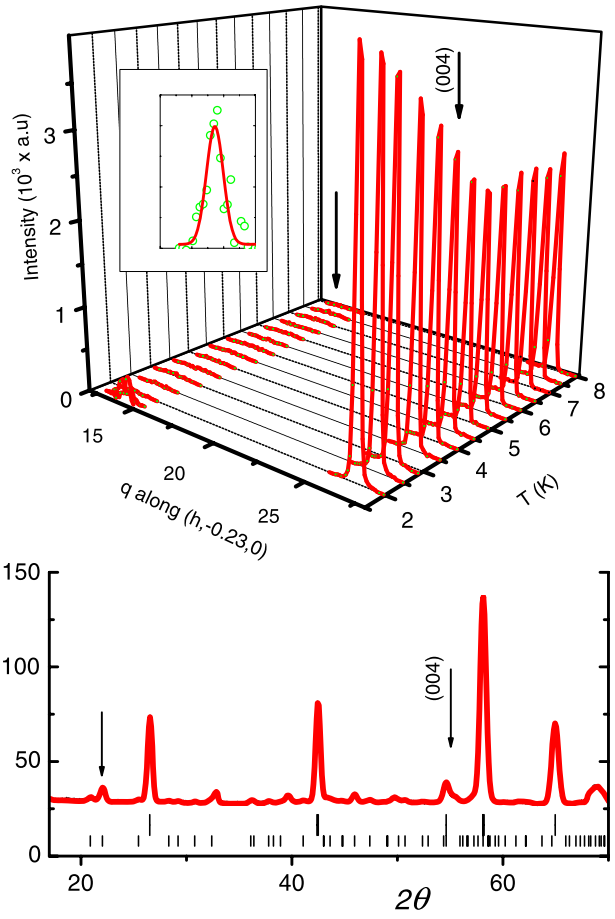

Figure 9. The upper panel shows, on a three-dimensional plot, the thermal evolution of the (0, 0, 4) peak and an impurity peak. The latter together with its Gaussian fit is shown, on an expanded scale, in the inset. The lower panel shows the powder diffractogram at 2 K (taken from figure 7). The intensities of the (0, 0, 4) and impurity peaks (marked by a vertical arrow) are almost equal in the powder diffractogram but are a factor of 20 different in the single-crystal diffractograms (no correction for multiplicity factors are considered). The wavelength used for the measurement in the upper panel is 2.3606 Å while for the lower panel it is 2.42 Å.

exhibited in the magnetostriction experiment of figure 4(a). On the other hand, figure 8(c) compares the reduced Tb magnetic moment, $\mu(T)/\mu(2\ {\rm K})$, with the calculated Brillouin function, $B_6(x)$ ($J = 6$, representing the total angular momentum quantum number of a free Tb^{3+} ion). Since, as shown above, there are considerable CEF effects, then this $B_6(x)$ curve should be taken as a limiting bound; nonetheless, the overall thermal evolution of $\mu(T)/\mu(2\ {\rm K})$ follows reasonably well this $B_6(x)$ curve; in particular, it reveals a smooth and monotonic evolution across the $T_{\rm m}$ region.

4. Discussion and conclusions

Although the Co 3d orbitals in YCo_2B_2C are not polarized, it may still be claimed that, due to the strong $H_{\rm eff}^{\rm Co}$, the 3d orbitals in $TbCo_2B_2C$ may undergo a spontaneous polarization. If that is the case, then there should be two magnetic transitions: one related to the R subsystem and another to the Co subsystem, such as in, for example, $Er_{0.6}Y_{0.4}Co_2$ [25]. As there are no spontaneous or field-induced metamagnetic transitions in any of the measured curves, particularly $M(H, T < T_{\rm c})$, then the possibility of a (spontaneously) polarized Co moment must be excluded. Such a non-polarized character of the Co sublattice is reminiscent of the ternary compounds $TbCo_2X_2$ (X = Si, Ge, B) (though, here, in contrast to $TbCo_2B_2C$, the Tb sublattice is arranged into an AF type-I structure) [5].

It is significant that the FM structure of $TbCo_2B_2C$ is drastically different from any of the reported AFM-type modes of the Ni-based borocarbides [16], in particular $TbNi_2B_2C$ [17, 21, 23, 26–28], even though both Tb-based isomorphs are similar in most (if not all) of the single-ion CEF-influenced properties such as the anisotropy, strength and orientation of the Tb moments (see sections 3.1 and 3.4). However, these isomorphs are distinctly different (see table 2) in their transition points, in their magnetic structures and in the overall features of their H–T phase diagrams (a simple one-boundary FM phase diagram versus another with a cascade of field-induced phase transitions). Based on the electronic structure calculation on $LuCo_2B_2C$ [8], these differences must be related to the difference in the details of their electronic structures (in particular the position of $E_{\rm F}$ within the $N(E)$ curve and the derived generalized susceptibilities). As a result, two consequences are expected: (i) those nesting features [29] that are responsible for the modulated mode in $TbNi_2B_2C$ must be absent in $TbCo_2B_2C$ and (ii) the effective Tb–Tb magnetic couplings must be different. To visualize the latter difference, let us recall that the indirect exchange coupling in metallic magnets is usually written as [30]

$$J(R_{ni}) = \frac{9\pi n^2 \Gamma^2 (g-1)^2}{8V^2 E_{\rm F}} F(2k_{\rm F}R_{ni}) \exp(-R_{ni}/\lambda),$$

$$F(x) = \left[\frac{x\cos(x) - \sin(x)}{(x)^4}\right],$$

where Γ is the s–f exchange coupling, n is the carrier concentration (governed by $N(E)$), R_{ni} is the distance separating the moments, $E_{\rm F}$ and $k_{\rm F}$ are the Fermi energy and

wavevector, and λ ($>R$) is the mean free path. Considering that these couplings manifest a quadratic dependence on n and a sinusoidal dependence on R_{ni}, then it is no surprise that the combination of difference in the position of E_F [8], and in the lattice parameters (see table 2) would lead to a strong difference in the magnitude and sign of the coupling constants and as such to a drastic difference in the magnetic properties. In fact, such a difference is not limited to these Tb-based isomorphs. Rather, our preliminary studies showed that this is valid for the whole RCo_2B_2C magnets [31]: as an example, the FM mode is observed in $TmCo_2B_2C$ [32] as well as in RCo_2B_2C (R = Ho, Dy) [31].

Acknowledgments

We acknowledge the partial financial support from the Brazilian agencies CNPq (485058/2006-5) and Faperj (E-26/171.343/2005).

Appendix. Magnon contribution from the ferromagnetic Tb sublattice of $TbCo_2B_2C$

The above-mentioned ferromagnetic order of the Tb sublattice suggests that the dominant exchange interactions within the same layer (approximated by a positive J_1) as well as those among different layers (approximated by a positive J_2) are ferromagnetic. Let us assume that the main contributions to the magnetic energy is due to the above-mentioned exchange couplings and anisotropic crystalline electric field interactions. Within the low-temperature regime of interest, the anisotropic interactions can be approximated by an effective field $\vec{H}_a$ (in energy units) which, for this particular case, forces the moments to points along the a axis. The Hamiltonian (under zero external field) can be written as

$$\mathcal{H} = -\sum_{i,j\epsilon A,B} J_1 \vec{S}_i \cdot \vec{S}_j - \sum_{\langle ij\rangle, i\epsilon A, j\epsilon B} J_2 \vec{S}_i \cdot \vec{S}_j - \vec{H}_a \cdot \sum_{i\epsilon A,B} \vec{S}_i . \tag{A.1}$$

All symbols have their usual meanings. The first term sums the bilinear products of two neighboring spins of the same layer A and afterward the contribution of all layers are added together. The second term sums all the bilinear product of two neighboring spins (each belong to a different but an adjacent layer). The third term is a sum over all single-ion anisotropy energies. Using the standard linear spin-wave approximation (considering a non-interacting magnon gas), equation (A.1) can be diagonalized to give the following dispersion relation:

$$\begin{aligned}\hbar\omega_k = {} & SJ_1(4 - 2\cos bk_x - 2\cos ak_z) \\ & + 2SJ_2\left\{4 - \cos\left(\frac{a}{2}k_z + \frac{b}{2}k_x + \frac{c}{2}k_y\right)\right. \\ & - \cos\left(-\frac{a}{2}k_z + \frac{b}{2}k_x + \frac{c}{2}k_y\right) \\ & - \cos\left(\frac{a}{2}k_z - \frac{b}{2}k_x + \frac{c}{2}k_y\right) \\ & \left. - \cos\left(\frac{a}{2}k_z + \frac{b}{2}k_x - \frac{c}{2}k_y\right)\right\} + H_a,\end{aligned}$$

where z (the quantization axis), x and y axes are, respectively, along the a (easy direction), b and c directions of the crystallographic unit cell. In the long-wave limit, up to second order, this simplifies to

$$\hbar\omega_k = \Delta + c_x k_x^2 + c_y k_y^2 + c_z k_z^2. \tag{A.2}$$

Assuming a weaker orthorhombic distortion ($a \approx b$ and $c_x \approx c_z$), one gets

$$c_x = Sa^2(J_1 + J_2) \equiv c_z$$

$$c_y = Sc^2 J_2.$$

The energy gap ($k = 0$) is

$$\Delta = H_a. \tag{A.3}$$

The expression for the density of states (obtained from integrating over the constant energy surface, $\epsilon \equiv \omega$) is

$$\rho(\epsilon) = \frac{V}{(2\pi)^3}\int \frac{\mathrm{d}S_\epsilon}{\mid \nabla\hbar\omega_k \mid} = \frac{V}{2\pi^2}\frac{\sqrt{\epsilon - \Delta}}{c_x\sqrt{c_y}a^2c}. \tag{A.4}$$

The magnon contribution to the total energy is

$$E = E_0 + \int_\Delta^\infty \mathrm{d}\epsilon \frac{\epsilon\rho(\epsilon)}{\mathrm{e}^{\beta\epsilon} - 1}$$

where E_0 is a constant independent of temperature. Using equations (A.2)–(A.4), the molar specific heat is (ν is the number of moles)

$$C_{\mathrm{mag}}(T) = \frac{1}{\nu}\frac{\mathrm{d}E}{\mathrm{d}T} = \frac{R}{2\pi^2 c_x\sqrt{c_y}}\frac{1}{T^2}\sum_{n=1}^{\infty} I_n,$$

where

$$\begin{aligned}I_n = {} & n\int_\Delta^\infty \mathrm{d}\epsilon\epsilon^2\sqrt{\epsilon - \Delta}\mathrm{e}^{-n\beta\epsilon} = 2n\mathrm{e}^{-n\beta\Delta}\left\{\frac{1\cdot 3\cdot 5\cdot\sqrt{\pi}}{2^4(n\beta)^{7/2}}\right. \\ & \left. + 2\Delta\frac{1\cdot 3\cdot\sqrt{\pi}}{2^3(n\beta)^{5/2}} + \Delta^2\frac{\sqrt{\pi}}{2^2(n\beta)^{3/2}}\right\}.\end{aligned}$$

The final result can be rearranged to give

$$\begin{aligned}C_{\mathrm{mag}}(T) = {} & \frac{15\cdot R\Delta^{\frac{3}{2}}}{8\cdot\pi^{\frac{3}{2}}D^{\frac{3}{2}}}\sum_{n=1}^{\infty} n.\exp\left(-\frac{n\Delta}{T}\right) \\ & \times\left[\frac{4}{15}\left(\frac{T}{n\Delta}\right)^{-\frac{1}{2}} + \left(\frac{T}{n\Delta}\right)^{\frac{1}{2}} + \left(\frac{T}{n\Delta}\right)^{\frac{3}{2}}\right]\end{aligned} \tag{A.5}$$

where

$$D = 2^{\frac{1}{3}}S(J_1 + J_2)^{\frac{2}{3}}J_2^{\frac{1}{3}}, \tag{A.6}$$

is the spin-wave stiffness coefficient [33] which is a measure of the effective coupling strength. This expression reproduces the high-temperature limit ($T \gg \Delta$):

$$C_{\mathrm{M}}(T) \propto \mathrm{e}^{-\Delta/T}T^{3/2},$$

which for $\Delta = 0$ gives the well-known $\frac{3}{2}$-Bloch expression [33]. At lower temperatures ($T \ll \Delta$), the strong dependence on the gap is emphasized:

$$C_{\mathrm{M}}(T) \propto \mathrm{e}^{-\Delta/T}T^{-1/2}.$$

References

[1] Bloch D and Lemaire R 1970 *Phys. Rev.* B **2** 2648
[2] Bloch D, Edwards D M, Shimizu M and Voiron J 1975 *J. Phys. F: Met. Phys.* **5** 1217
[3] Cyrot M and Lavagna M 1979 *J. Physique* **40** 763
[4] Cyrot M, Gignoux D, Givourd F and Lavagna M 1979 *J. Physique* **40** C5
[5] Szytula A and Leciejewicz J 1994 *Handbook of Crystal Structures and Magnetic Properties of Rare Earth Intermetallics* (Boca Raton, FL: CRC Press)
[6] Müller K-H and Narozhnyi V N 2001 *Rep. Prog. Phys.* **64** 943
[7] El Massalami M, Borges H A, Takeya H, Rapp R E and Chaves A 2004 *J. Magn. Magn. Mater.* **279** 5
[8] Coehoorn R 1994 *Physica* C **228** 331
[9] Lee J I, Zhao T S, Kim I G, Min B I and Youn S J 1994 *Phys. Rev.* B **50** 4030
[10] Matthias L F 1994 *Phys. Rev.* B **49** 13279
[11] Pickett W E and Singh D J 1994 *Phys. Rev. Lett.* **72** 3702
[12] ElMassalami M, DaCosta M S, Rapp R E and Chaves F A B 2000 *Phys. Rev.* B **62** 8942
[13] El Massalami M, Chagas E F and Rapp R E 2001 *J. Magn. Magn. Mater.* **226–230** 1058
[14] Takeya H, Habuta E, Kawano-Furukawa H, Ooba T and Hirata K 2001 *J. Magn. Magn. Mater.* **226** 269
[15] ElMassalami M, Amara M, Galera R-M, Schmitt D and Takeya H 2007 *Phys. Rev.* B **76** 104410
[16] Lynn J W, Skanthakumar S, Huang Q, Sinha S K, Hossain Z, Gupta L C, Nagarajan R and Godart C 1997 *Phys. Rev.* B **55** 6584
[17] Cho B K, Canfield P C and Johnston D C 1996 *Phys. Rev.* B **53** 8499
[18] Moon R M, Koehler W C and Farrell J 1965 *J. Appl. Phys.* **36** 978
[19] Kruis M, Pickett G R and Veuro M C 1969 *Phys. Rev.* B **177** 910
[20] Song C, Islam Z, Lottermoser L, Goldman A I, Canfield P C and Detlefs C 1999 *Phys. Rev.* B **60** 6223
[21] Song C, Wermeille D, Goldman A I, Canfield P C, Rhee J Y and Harmon B N 2001 *Phys. Rev.* B **63** 104507
[22] Song C, Lang J C, Detlefs C, Letoublon A, Good W, Kim J, Wermeille D, Bud'ko S L, Canfield P C and Goldman A I 2001 *Phys. Rev.* B **64** 20403
[23] Detlefs C, Song C, Brown S, Thompson P, Kreyssig A, Budko S L and Canfield P C 2003 arXiv:cond-mat/0306742
[24] Rodríguez-Carvajal J 1993 *Physica* B **192** 55
[25] Hauser R, Bauer E, Gratz E, Müller H, Rotter M, Michor H, Hilscher G, Markosyan A, Kamishima K and Goto T 2000 *Phys. Rev.* B **61** 1198
[26] Tomy C V, Afalfiz L A, Lees M R, Martin J M, McK Paul D and Adroja D T 1996 *Phys. Rev.* B **53** 307
[27] Dervenagas P, Zarestky J, Stassis C, Goldman A I, Canfield P C and Cho B K 1996 *Phys. Rev.* B **53** 8506
[28] Kreyssig A, Stockert O, Dreyhaupt A, Ressouche E, Ritter B G C, Bitterlich H, Behr G, Canfield P C and Loewenhaupt M 2003 *J. Low Temp. Phys.* **131** 1129
[29] Rhee J Y, Wang X and Harmon B N 1995 *Phys. Rev.* B **51** 15585
[30] Coqblin B 1977 *The Electronic Structure of Rare-Earth Metals and Alloys: the Magnetic Heavy Rare-Earth* (New York: Academic)
[31] ElMassalami M, Moreno R, Takeya H, Ouladdiaf B, Lynn J W and Freitas R S 2009 *J. Phys.: Condens. Matter* submitted
[32] ElMassalami M, Rapp R E, Chaves F A B, Moreno R, Takeya H, Ouladdiaf B, Lynn J W, Huang Q, Freitas R S and Oliveria N F Jr 2009 *J. Phys.: Condens. Matter* **21** 046007
[33] Kittel C 1963 *Quantum Theory of Solids* (New York: Wiley)